Available online at www.sciencedirect.com
ScienceDirect
Journal of Power Sources 174 (2007) 272–281
JOURNAL OF POWER SOURCES
www.elsevier.com/locate/jpowsour

Current distribution in polymer electrolyte membrane fuel cell with active water management

Daniel G. Strickland, Shawn Litster, Juan G. Santiago *

Department of Mechanical Engineering, Stanford University, Stanford, CA 94305, USA

Received 20 June 2007; received in revised form 16 August 2007; accepted 16 August 2007
Available online 28 August 2007

Abstract

Air delivery is typically the greatest parasitic power loss in polymer electrolyte membrane fuel cell (PEMFC) systems. We here present a detailed study of an active water management system for PEMFCs, which uses a hydrophilic, porous cathode flow field, and an electroosmotic (EO) pump for water removal. This active pumping of liquid water allows for stable operation with relatively low air flow rates and low air pressure and parallel cathode channel architectures. We characterize in-plane transport issues and power distributions using a three by three segmented PEMFC design. Our transient and steady state data provide insight into the dynamics and spatial distribution of flooding and flood-recovery processes. Segment-specific polarization curves reveal that the combination of a wick and an EO pump can effect a steady state, uniform current distribution for a parallel channel cathode flow field, even at low air stoichiometries ($\alpha_{air} = 1.5$). The segmented cell measurements also reveal the mechanisms and dynamics associated with EO pump based recovery from catastrophic flooding. For most operating regimes, the EO pump requires less than 1% of the fuel cell power to recover from near-catastrophic flooding, prevent flooding, and extend the current density operation range.

Keywords: PEM fuel cell; Electroosmotic pump; Segmented cell; Parallel flow; Water management; Wick

1. Introduction

Increasing energy demands of new, high performance portable electronic devices are outpacing advances in battery technology [1] and new high energy density power sources are required. Polymer electrolyte membrane fuel cells (PEMFCs) are a promising alternative with potential for significantly increased energy density. Another important sector is power sources for vehicles. Growing environmental concerns spur the development of clean energy alternatives and PEMFCs have been a favored technology as they provide emissions-free power, while operating at high efficiency. Integration into on-board power systems, however, remains a challenge. Air pressurization and delivery are particularly challenging as on-board compressors add to system complexity and can make start-up more difficult [2]. Air delivery parasitic losses are also problematic during vehicle idle where air delivery may require a significant portion of the total power required to keep the fuel cell and auxiliary systems operating [3].

Leveraging parallel channel architectures for PEMFC cathodes can minimize air delivery parasitic power losses, as parallel channels require lower pressure differentials and thereby eliminate the need for high air compression. Parallel flow fields also offer improved transient performance reliability [4] and simplified flow field manufacturing processes [5]. Despite these benefits, parallel flow fields are seldom used as they are particularly susceptible to flooding [6]. Flooding is addressable in parallel channels, but this is typically accomplished by using very high air stoichiometries ($\alpha_{air} = 4$–5 [5]) to advectively remove product water; and this approach again results in significant parasitic power losses [7].

Several groups have explored novel water management structures and methods including manifold designs that evenly distribute air flow, cooling channel designs that optimize planar temperature gradients for controlled relative humidity, and porous bipolar plates that distribute and remove product water [8–10]. We recently presented a water management technique that eliminated the need for excessive air flow rates by integrat-

* Corresponding author. Tel.: +1 650 723 5689; fax: +1 650 723 7657.
E-mail address: juan.santiago@stanford.edu (J.G. Santiago).

0378-7753/$ – see front matter © 2007 Elsevier B.V. All rights reserved.
doi:10.1016/j.jpowsour.2007.08.059

ing a low power pump to directly remove water from cathode channels and the gas diffusion layer of PEMFCs (see Litster et al. [11]). This system employed a porous carbon cathode flow field and coupled electroosmotic (EO) pump for water removal from a 25 cm^2 fuel cell. Results showed consistent, flood-free performance at air stoichiometries as low as $\alpha_{air} = 1.3$, and the EO pump required < 1% of fuel cell power. In this paper we leverage the segmentation of the anode of the 25 cm^2 fuel cell described by Litster to gain new insight into water transport in this active water management system. Cell segmentation provides measurements of local current density within the fuel cell. Such data provides insight into localized phenomena including oxygen depletion at the cathode and flooding events.

Segmentation is a unique diagnostic tool for examining spatially and temporally resolved flooding events. Mench et al. [12] used cell segmentation to observe current density as a function of streamwise length in a serpentine channel cathode flow field. They observed decreased current density near the cathode outlet, with losses intensifying at low air flow rates. These power losses were attributed to liquid water accumulation in the GDL. Yoon et al. [13] investigated flooding effects using a segmented cell (nine by nine segments) with a triple serpentine cathode and single serpentine anode flow field. Yoon induced cell flooding by increasing gas inlet relative humidity. Similar to Mench et al., flooding was observed first near the cathode outlet and then continued toward the inlet until a steady state condition was reached. Although cell segmentation has been conducted in these and other cell configurations [13–28], few studies have examined parallel cathode flow field architecture and, to the best of our knowledge, no studies have investigated current distribution with porous carbon media for cathode flow fields. Our work is therefore the first segmented anode study of a porous carbon cathode, with and without active water management.

2. Experimental

2.1. Fuel cell assembly and operating conditions

As described above, our design is based on the 25 cm^2 PEMFC design presented by Litster et al. [11]. The fuel cell assembly, including the segmented anode components introduced in this paper, is shown schematically in Fig. 1. Assembly endplates were machined from aluminum (McMaster-Carr, Atlanta, GA), and were equipped with Kapton heaters and K-type thermocouples for temperature control. Aluminum end plates were electrically insulated from the current collectors with a 0.5 mm thick silicone rubber layer. The fuel cell was equipped with cathode-side water management flow field, and a segmented anode flow field and current collector. We describe the latter components in the next two sections.

We used a commercially available catalyst coated membrane electrode assembly (MEA), obtained from Ion Power Inc. (Newcastle, DE). Four 1/4 in.-20 bolts tightened to 35 in.-lb were used for compression. For all experiments, we operated the fuel cell at a temperature of 55 °C. Inlet gas dew points were also 55 °C. Hydrogen flow rate was $\alpha_{H_2} = 2.0$. The system components and fuel cell operating conditions are summarized in Table 1. Further details regarding the MEA, cathode flow field, and supporting systems (e.g., air and fuel delivery) are given by Litster et al.

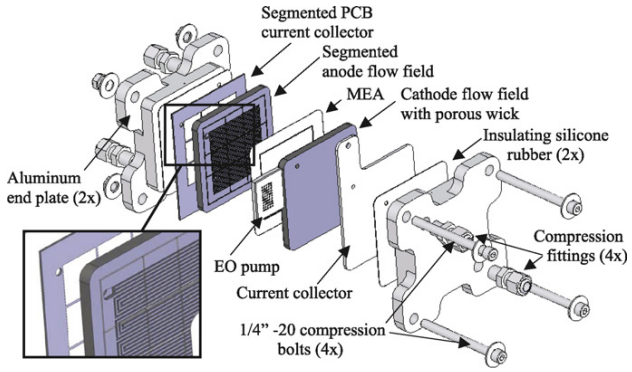

Fig. 1. Schematic of 25 cm^2 PEMFC assembly. Fuel cell features a porous carbon cathode flow field with coupled EO pump for water management, and segmented anode-side current collector and flow field for current distribution measurements. Membrane is a commercially available catalyst coated MEA (Ion Power Inc, Newcastle, DE), with Teflon gasket for sealing. Silicone rubber electrically insulates current collectors from aluminum end plates. Four bolts tightened to 35 in.-lb provide cell compression.

2.2. Cathode flow field for active water management

We here summarize the design of the cathode flow field with integrated water management; further details are given by Litster. As shown in Fig. 2a, a parallel flow field was machined from porous carbon (SGL SIGRACET-plate PGP material, SGL Technologies GmbH, Germany), which was then heat treated (baked at 300 °C for 3 min) for increased hydrophilicity. The porous carbon was then seated into a non-porous graphite base. A small (1 cm × 2 cm) tab of the porous carbon layer extends out of the assembly, and this external wick region is coupled to the electroosmotic pump assembly. The electroosmotic pump assembly consists of (starting from above the cathode region and in the major pump flow direction as shown in Fig. 2b) an acrylic frame, a mesh platinum pump anode, a hydrophilic poly-vinyl alcohol (PVA) filter component, a porous borosilicate glass frit

Table 1
Summary of fuel cell system components and operating conditions

Parameter	Value
Membrane electrode assembly	Ion Power CCM
Membrane thickness	25 μm
Platinum loading	0.3 mg Pt cm^{-2}
Gas diffusion layer	SGL 10-BB (non-woven w/MPL)
Fuel cell active area	25 cm^2
Anode gas	H_2 (>99.995%)
Anode dew point	55 °C
Hydrogen stoichiometry	2.0
Air stoichiometries	1.3–6.0
Cathode gas source	Air (extra dry)
Cathode delivered air dew point	55 °C
Endplate temperatures	55 °C
Gas line temperatures	60 °C
Electroosmotic pump area	2 cm^2
Electroosmotic pump voltage	12 V (unless noted otherwise)

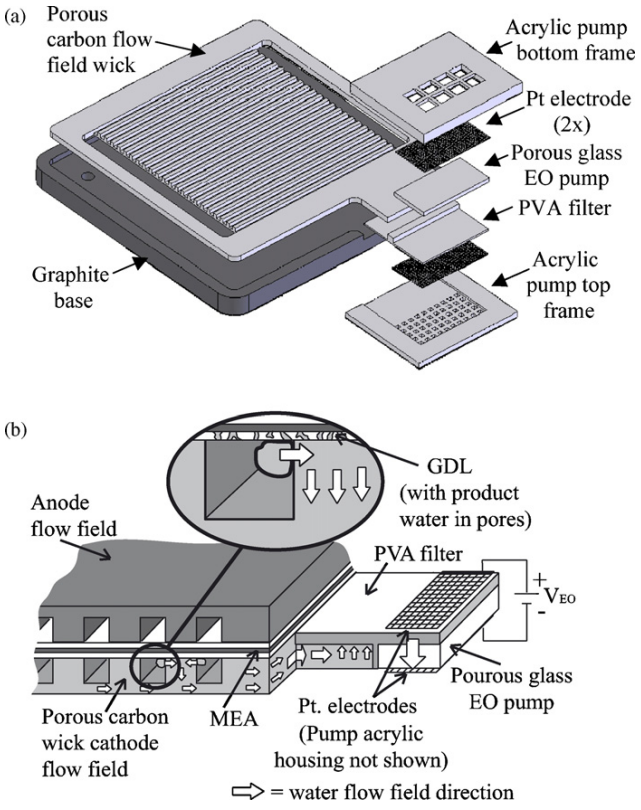

Fig. 2. (a) Exploded assembly view of water management system on cathode-side featuring 25 cm^2 porous carbon flow field and 2 cm^2 EO pump, and (b) schematic of water flow through porous carbon wick to the EO pump. The hydrophilic porous carbon flow field absorbs product water from the GDL and functions as a current collector. The EO pump provides a pressure gradient, which pulls water from the flow field, pumps it through the PVA filter, and rejects it externally. White arrows show direction of water flow.

(glass filter from Robu-Glas, Germany), a mesh platinum pump cathode, and a second acrylic frame. The pump hydraulically couples to the porous carbon wick through the PVA filter component, which helps electrically isolate the pump and serves as a filter, keeping particles (e.g., carbon) out of the pump. The acrylic frames add support and the electrodes are attached via wire clamps to external steel wire leads. When dry, the wick and pump initially act as a passive wick, which removes water from the cathode channels and SGL (see Fig. 2b). Once these porous components are saturated with fuel cell product water, the pump's electrochemical circuit is automatically closed and the pressure differential generated by the EO pump creates a slight local vacuum in the PVA filter. This local vacuum extracts product water from the fuel cell wick, and this product water is then pumped out by the EO pump.

2.3. Segmentation

2.3.1. Segmentation techniques

Segmentation methods were initially developed to examine local effects of evolving gases and mass transport losses in electrolytic cells [29,30]. Cleghorn et al. [16] first adapted segmentation for current distribution measurements in PEMFCs using printed circuit board (PCB) technology to fabricate a segmented anode flow field and current collector. Stumper et al. [26] published an early paper examining three methods of segmentation: partial MEA, sub-cells, and current mapping. The partial MEA method employed a partially catalyzed membrane that limited electrochemical reaction to specific areas within the fuel cell plane. Several MEAs with progressively more area catalyzed were used to construct the spatially resolved current distribution. The sub-cell method involved creating one or more small electrically isolated islands within the cell. The measured current of these islands provided localized current information. The current mapping technique used a passive resistor network, inserted between the flow field plate and the current collecting bus, to measure current distribution in the fuel cell plane.

Bender et al. [14] refined the cell segmentation technique by segmenting the entire anode side of the fuel cell including the electrode, GDL, flow field, and current collector. Bender also carefully calibrated contact resistances throughout the flow field and used Hall sensors for low impedance, *ex situ* current measurements. These efforts resulted in a reduction of error due to lateral currents; and the group demonstrated real time measurements of current distribution. Continuing work in the area of fuel cell segmentation has focused on stack integration [19,27], application to larger scale fuel cell systems [31], implementation of segment-specific electrochemical impedance spectroscopy [25], and increase of spatial resolution. Recently, Freunberger et al. [17] demonstrated sub-millimeter resolution, providing insight into mass transport issues in land and channel areas of the flow field plate. In this work, we segment the anode flow field plate and current collector into a three by three array. We leave the MEA and GDL undisturbed and unsegmented to minimize the invasiveness of cell segmentation.

2.3.2. Fabrication

An anode flow field with three by three segmentation was fabricated as shown in Fig. 3. The process for isolating sections of the anode is similar to that reported by Schneider et al. [25]. Grooves, 1 mm wide × 3 mm deep were machined into a 70 mm × 70 mm × 5 mm graphite block (Fuelcellstore.com, Boulder, CO) and then filled with an electrically insulating resin (6366K41, McMaster-Carr, Atlanta, GA). After curing at room temperature for 24 h, the surface was hand sanded to a smooth finish. We then faced (end milled) the block from the side opposite the milled sectioning grooves to a thickness of 2 mm, leaving nine electrically isolated segments. A three-channel serpentine flow field pattern was then end milled into the front of the block. These channels had channel width, channel depth and rib thickness of 0.75 mm.

A printed circuit board (PCB) segmented current collector was designed and manufactured using a custom, rapid manufacturing protocol (ExpressPCB^{TM}) as shown in Fig. 4. Nine 16.3 mm × 16.3 mm, 43 μm thick copper pads were printed in a three by three array on the top side of the PCB. Four small thru vias connect each pad to a printed lead on the backside of the board; and these leads electrically join each segment to a connector array (header) for connection to the data acquisition

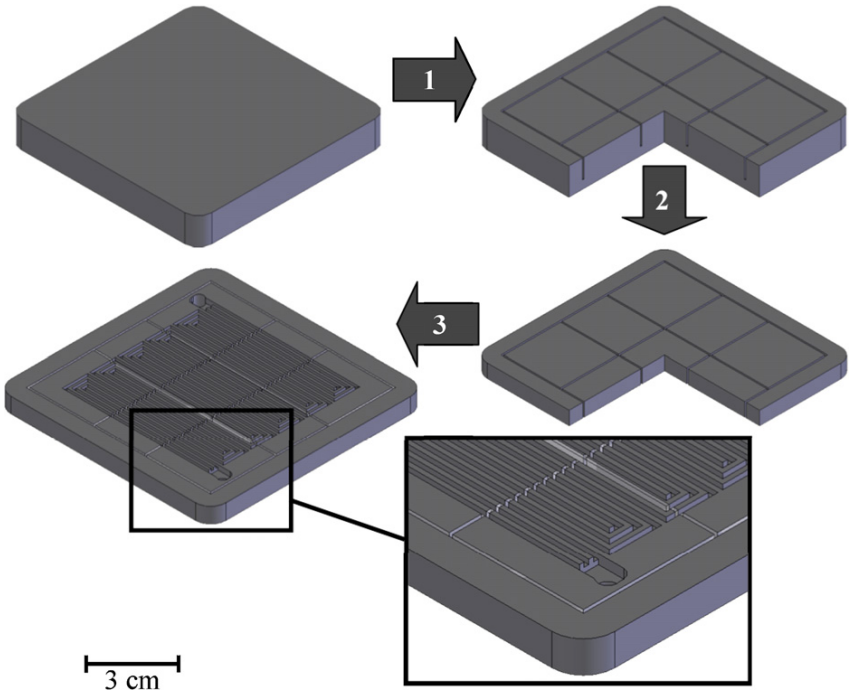

Fig. 3. Fabrication process for segmented anode flow field plate. (1) We machined grooves (1 mm width, 3 mm depth) into a 70 mm × 70 mm × 5 mm graphite block. We then filled the grooves with a low viscosity epoxy resin and let set at room temperature for 24 h. (2) Next, we hand sanded the top side to a smooth finish and faced (end milled) the backside to a total thickness of 2 mm, thereby electrically isolating the nine segments. (3) We then machined a three-channel serpentine flow field into the top face of the block.

instrumentation. After receiving the PCB from ExpressPCB, we electroplated the copper pads and leads with a 10 μm nickel diffusion barrier and 1 μm gold layer (Electrochem, Inc., Union City, CA). A 0.5 mm thick silicone–rubber layer between the end plate and the PCB board (see Fig. 1) prevented electrical shorts between leads.

2.4. Flow field configuration

Fig. 5 shows a schematic of the segmented anode flow field and the porous cathode flow field with a hydraulically coupled, external EO pump. Air entered near segment one, traveled through the porous carbon 23-channel parallel flow field plate and exited near segment nine. Hydrogen entered near segment nine, traveled through the triple serpentine segmented flow field and exited near segment one. The EO pump was positioned near segments six and nine, near the cathode outlet, in order to minimize hydraulic resistance between the pump and the areas most susceptible to flooding.

2.5. Instrumentation

A schematic of the segmented cell instrumentation is shown in Fig. 6. Electrical current flows to each of the nine anode segments. We used low impedance (specification by manufacturer of 0.18 mΩ) Hall effect current sensors (LAH-25NP, LEM, Switzerland) to measure current in each channel. Minimizing impedance of the measuring circuit reduces lateral potential differences along the cell area (which can cause unwanted lateral currents). We mounted the Hall sensors on a PCB and electroplated the leads with 180 μm silver (Electrochem, Inc., Union City, CA) to further reduce impedance. These sensors output

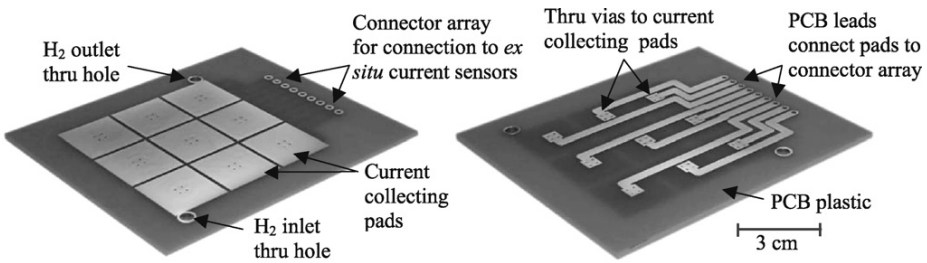

Fig. 4. Images of both sides of the printed circuit board segmented current collector. Nine 16.3 mm × 16.3 mm pads were printed on the front side of the board for contact with graphite flow field segments. Four small thru vias electrically connect each pad to a lead on the backside of the board, which connect to a linear array for connection to instrumentation. We electroplated the PCB leads and contact pads with a 10 μm nickel diffusion layer and 1 μm gold layer.

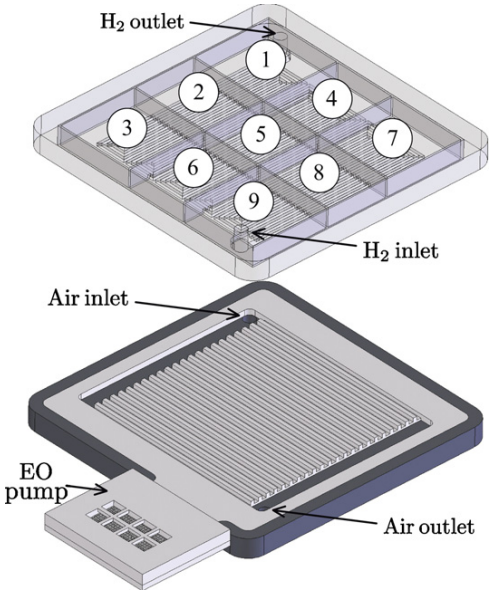

Fig. 5. Flow field configuration for all experiments. Shown are the nine segments of the anode plate and the cathode assembly including air flow field channels and the EO pump. The anode and cathode employed a triple serpentine and 23-channel parallel flow configuration, respectively. Also shown are the inlets and outlets for hydrogen and air.

a measurement current proportional to the conducted signal current, which we converted to a measured potential difference using 1 kΩ precision resistors. We used a PCI-6031E data acquisition card and LabView software for all measurements (National Instrument, Austin, TX). The nine Hall sensor outputs were connected in parallel to the electronic load (Agilent N3301A, Santa Clara, CA), which was in series with the fuel cell cathode.

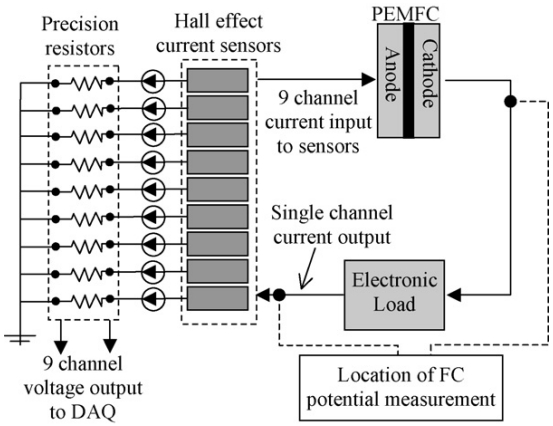

Fig. 6. Diagram of cell instrumentation. Electric current travels to the anode current collector thru nine parallel channels, each fitted with a Hall effect current sensor. The Hall sensors output a current proportional to the measured current, which is converted to a measured potential via 1 kΩ precision resistors. The nine channels are connected in parallel to the electronic load, which is connected in series with the fuel cell cathode. Cell potential is measured across the electronic load.

2.6. Impedance calibration

To ensure uniformity of contact resistance, we compressed the current collector in series with the segmented graphite flow field, gas diffusion layer and a copper plate. We then measured impedance through each segment, from PCB lead to copper plate, using the highly sensitive four-wire method and a sourcemeter (Keithley 2400 Sourcemeter, Cleveland, OH). Our mean segment impedance and standard deviation was 15.5 and 2.84 mΩ, respectively. We attribute the variation in segment impedance to differences in current collector PCB lead lengths. The maximum neighboring segment percent voltage difference due to non-uniform impedance was approximately 4.0% at a total-area-averaged current density of $\bar{I} = 1\,\mathrm{A\,cm^{-2}}$. The latter is the normalized maximum percent voltage difference between segments due to segment impedance differences (assuming uniform current distribution); calculated as $(\Delta R_{\max}/V_{\mathrm{cell}})(I_{\mathrm{tot}}/N)\cdot 100\%$. Here $\Delta R_{\max}$ is the maximum impedance difference between neighboring segments, I_{tot} the total operating current, N the number of segments, and V_{cell} is the approximate cell voltage for the given I_{tot}. Note that actual percentage voltage difference between neighboring segments will in practice exceed the estimate above, as segment voltage difference is also a function of the instantaneous current density in each segment. As shown by our measurements below, neighboring cells often experience relatively large differences in current density (as high as 750 mA cm^{-2} differences). Accordingly, the metric given above, which assumes uniform current density, is useful only as a measure of resistance uniformity, and should not be interpreted as the actual voltage difference between segments contributing to cross currents.

Using the current interrupt method, we measured the ohmic impedance of the segmented cell as 8.10 mΩ. This is an increase of 1.25 mΩ over the measured impedance of the same fuel cell without cell segmentation (see Litster et al. [11]). We use this increase as an estimate of the impedance contributed by segmentation (including flow field segmentation, PCB current collector, measurement leads and current sensors). This results in an area specific resistance change due to segmentation of 31.3 mΩ cm^2 and an average segment measuring impedance increase of 11.3 mΩ.

Overall, we expect some current spreading due to measurement impedance, particularly under non-uniform current distribution operating conditions (see Eckl et al. [32]). However, the degree of error is non-prohibitive in qualitative current distribution characterization.

3. Results and discussion

3.1. Steady state

Polarization curves for the segmented fuel cell operated at stoichiometries between 1.3 and 6.0 are shown in Fig. 7. In these first plots, we show the sum total current from all segments in the cell without EO pumping and with EO pumping at $V_{\mathrm{EO}} = 12$ V. We obtained each polarization curve by increasing overall current density by 0.1 A cm^{-2} every 10 min. Voltages shown are

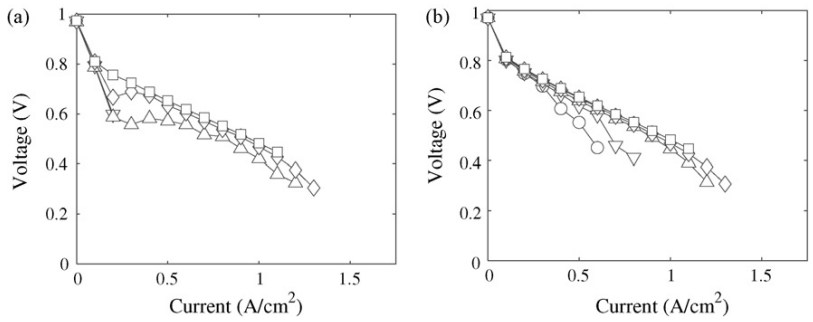

Fig. 7. Polarization curves showing total fuel cell performance for different stoichiometries, with (a) EO pump off and (b) EO pump on. Data are shown for stoichiometries of $\alpha_{air} = 1.3$ (◯), 1.5 (▽), 2.0 (△), 3.0 (◊), and 6.0 (□). Total cell current was held constant during each 10 min dwell time. Data points represent the time average of the last 2 min of data for each current increment. Without EO pumping, flooding prevents fuel cell operation at $\alpha_{air} = 1.3$ for all current densities, and prevents operation at $\alpha_{air} = 1.5$ for current densities above $\bar{I} = 0.2\,A\,cm^{-2}$. With EO pumping, fairly robust fuel cell operation is achieved at these low stoichiometries.

the average of the last 2 min of data collected for each 10 min dwell time. Before each polarization curve, we operated the fuel cell at a total-area-averaged current density, $\bar{I}$, of 0.8 A cm^{-2} for 10 min and then purged using high air flow rates to ensure consistent membrane hydration and a flood-free start condition. We terminated polarization curve measurements when the instantaneous cell voltage dropped below 0.2 V. We provide here only a brief description of the performance of the system with EO pumping and refer the reader to Litster et al. [11] for a detailed study of this identical cathode wick and EO pump design. Litster includes detailed comparisons between this and two control designs: A second design with a wick but no EO pumping, and a third design with a solid graphite plate cathode (and no EO pumping). Consistent with the work of Litster et al., the current results show that fuel cell operation was flood-free with EO pumping for stoichiometries of $\alpha_{air} = 2$–6, and flooding was significantly mitigated for $\alpha_{air} \leq 1.5$. Parasitic EO pump power consumption was nominal, ranging between 0.2 and 1% of total fuel cell power production for most operating regimes. This excludes very low operating current densities ($\bar{I} \leq 0.1\,A\,cm^{-2}$), where percent power consumption increased to 1–2%.

Segment-specific polarization curves for air stoichiometries of $\alpha_{air} = 1.5$–3.0 are shown in Fig. 8. For each operating air stoichiometry, polarization curves without EO pumping and with EO pumping at $V_{EO} = 12$ V are shown. For $\alpha_{air} \leq 2.0$, EO pumping significantly extended the operating range of the fuel cell and/or increased maximum power density. With no EO pumping and $\alpha_{air} = 1.5$, 2.0 and 3.0, the max power densities (averaged over the entire area) were 120, 420 and 470 mW cm^{-2}, respectively. In comparison, for EO pumping at 12 V, the respective max power densities were 350, 440 and 470 mW cm^{-2}. As expected, pumping had the strongest effect for low stoichiometries. At $\alpha_{air} = 1.5$, the case without EO pumping resulted in severe flooding at low current densities. For example, for the $\alpha_{air} = 1.5$ case, the current density for many of the segments dropped dramatically near current densities of 0.2 A cm^{-2}; indicative of catastrophic flooding. In contrast, with EO pumping, the fuel cell performance range was extended past current density values of 0.8 A cm^{-2}.

The data also show important spatial trends associated with flooding and the role of the EO pump in preventing flooding. We here first describe global trends and later discuss the specific cases. For $\alpha_{air} \geq 2.0$ and with EO pumping, current densities were highest in upstream segments and lowest in downstream segments. As a result, for each stoichiometry, polarization curves grouped into three distinct regions – high current, mid current and low current density – corresponding to upstream, midstream and downstream (with respect to cathode flow field) segments. We attribute this result to the reduction in oxygen partial pressure as oxygen is consumed at the cathode. Further, as air stoichiometry increased, the differences between segment groups systematically decreased. For $\alpha_{air} = 2.0$, 3.0 and 6.0, the segment-to-segment standard deviations of segment current densities, at a mean current density of 1.0 A cm^{-2}, were 0.132, 0.097, 0.070 A cm^{-2}, respectively. This trend is consistent with the expected increase in homogeneity of oxygen partial pressure as air stoichiometry increases.

We next discuss the challenging operation condition of $\alpha_{air} = 1.5$. At this low stoichiometry and with no EO pumping, nearly all segments clearly experience severe flooding at current densities above 0.1 A cm^{-2}. The maximum achievable current density was $\bar{I} = 0.2\,A\,cm^{-2}$. Activation of the EO pump extended the operating range and the maximum achievable $\bar{I}$ to 0.8 A cm^{-2}. For the latter case, the most severe flooding was limited to segments 4, 7, and (to a lesser degree) 1. These segments are positioned furthest from the EO pump. We conclude that at these current densities, the EO pump was unable to remove all excess product water and, as a result, channels far from the EO pump were left to flood.

At $\alpha_{air} = 2.0$, the case without EO pumping resulted in severe flooding for current densities between $\bar{I} = 0.2$ and 0.7 A cm^{-2}. Flooding effects were less pronounced for current densities beyond $\bar{I} = 0.7\,A\,cm^{-2}$. We attribute this mid-range current density flooding and subsequent recovery at higher current densities to the effects of passive water removal by the wick. For these fixed α_{air} curves, high current density implies higher air flow rate. As discussed by Litster et al., the cathode channel flow, the wick, and EO pump system act together to remove water. For the EO pump placement considered here, pressure gradients in the cathode channel translate to in-plane pressure gradients in the wick. These pressure gradients provide a driving force that helps pump water through the wick and toward

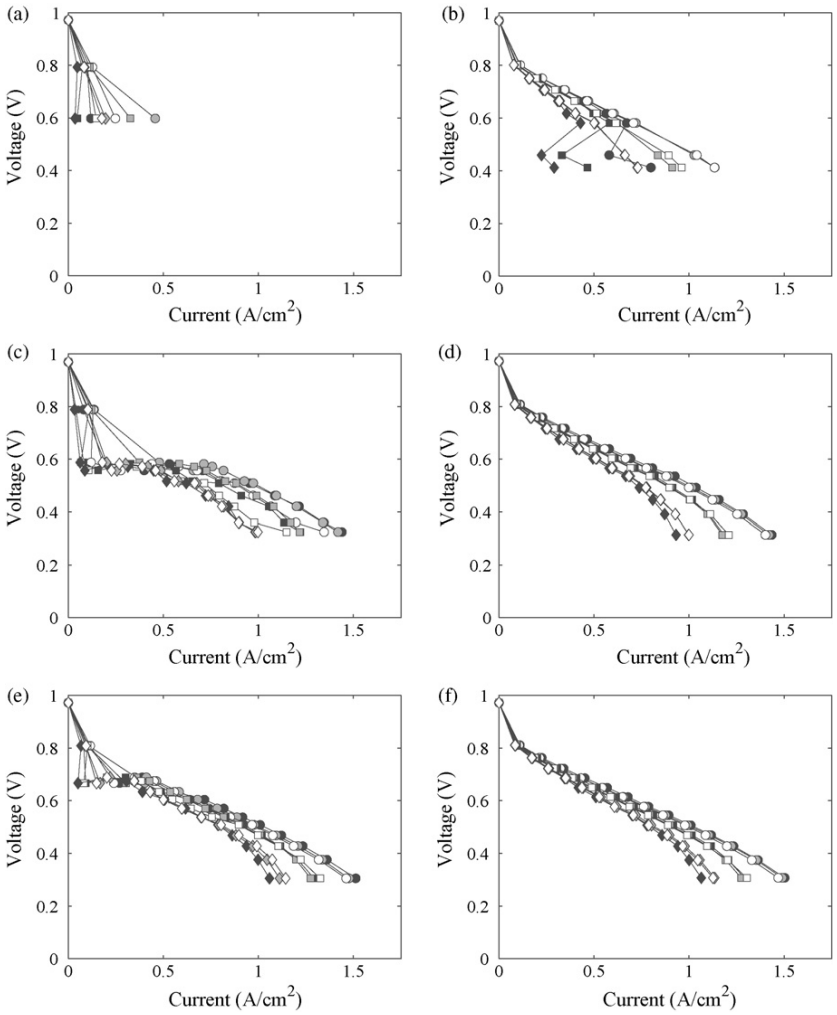

Fig. 8. Polarization curves with EO pump off (left) and EO pump on at $V_{EO} = 12$ V (right) for air stoichiometries of $\alpha_{air} = 1.5$ (a and b), $\alpha_{air} = 2.0$ (c and d), and $\alpha_{air} = 3.0$ (e and f). Segment locations are shown in Fig. 5, and are labeled as segments 1 (●), 2 (●), 3 (◯), 4 (■), 5 (■), 6 (□), 7 (♦), 8 (♦), and 9 (◇). EO pumping resulted in significant enhancement (extension) of the range of performance for low air stoichiometry, and flood-free performance at higher stoichiometries.

the EO pump and outlet. At the highest maximum current density value ($\bar{I} = 1.2\,A\,cm^{-2}$), the segment current densities again segregated into three groups corresponding to upstream, midstream and downstream segments, suggesting that at this high current operating condition, flooding was not significant. With EO pumping, the fuel cell also achieved a current density of $\bar{I} = 1.2\,A\,cm^{-2}$. We note that fuel cell operation was flood-free when the EO pump was activated. EO pumping eliminated the flooding observed during low current density operation. The low current density operating regime is of general interest. For example, stable, flood-free low current operation is desirable in automotive applications during vehicle idle, where auxiliary systems are the primary fuel cell load. Accordingly, GM/NIST [33] recently published a paper where they investigate fuel cell stack flooding at an operating current of $0.2\,A\,cm^{-2}$. Ahluwalia et al. [3] also showed fuel cell performance optimization at low power density to be essential for high overall efficiency. We conclude that EO pumping resulted in a meaningful improvement in fuel cell performance for $\alpha_{air} = 2.0$.

At $\alpha_{air} = 3.0$ and without EO pumping, the sharp drops in fuel cell voltage indicative of flooding were observed at current densities of $\bar{I} = 0.2$ and $0.3\,A\,cm^{-2}$, and primarily in the outlet header and outer channels. For currents higher than about $\bar{I} = 0.4\,A\,cm^{-2}$, the fuel cell again recovers from flooding. We again attribute this to the transport of water through the wick due to pressure gradients in the cathode channels. At this high α_{air}, high current density regime, product water is largely removed passively by the wick and we therefore expect no significant improvements from EO pumping. Above $\bar{I} = 0.7\,A\,cm^{-2}$, the segment current densities again segregate into distinct groups of upstream, midstream and downstream segments. In the case with EO pumping, as with $\alpha_{air} = 2.0$, we see no signs of flood-related mass transport losses throughout the regime of operation.

Lastly, in Fig. 9 we present polarization curves for the case of $\alpha_{air} = 1.3$ and with EO pumping at 12 V. We first note that without EO pumping, this low α_{air} case resulted in catastrophic flooding at $\bar{I} = 0.1\,A\,cm^{-2}$ and therefore no polarization curve could be obtained. These data therefore document fuel cell operation

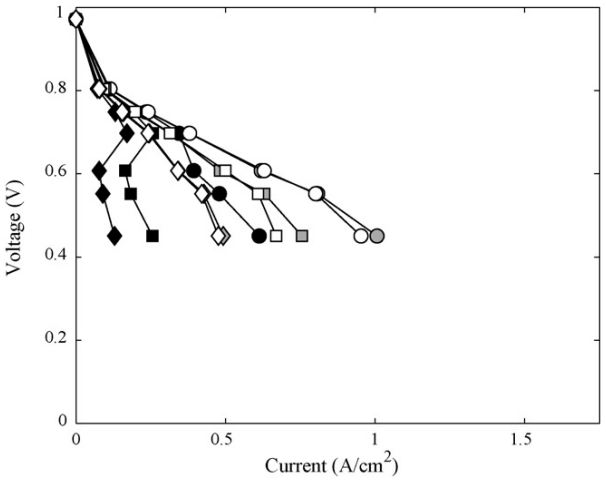

Fig. 9. Segment-specific polarization curves for $\alpha_{air} = 1.3$ and EO pumping at 12 V. Segment locations are shown in Fig. 5, and are labeled as segment 1 (●), 2 (●), 3 (○), 4 (■), 5 (■), 6 (□), 7 (♦), 8 (♦), and 9 (◇). Catastrophic flooding prevented measurement of a polarization curve at this low air stoichiometry, without EO pumping. Accordingly, all of the data shown here represent operating conditions enabled by EO pumping. Segments located far from the EO pump experienced the most significant losses due to flooding. Catastrophic flooding prevented operation beyond $\bar{I} = 0.5\,A\,cm^{-2}$.

regimes that are accessible only with EO pumping. Operation at $\alpha_{air} = 1.3$ is possible, but EO pumping provides insufficient water management at the chosen pump voltage. At this extremely low air stoichiometry case, pressure differences in the cathode are negligible (we estimate less than 400 Pa difference between inlet and outlet). Channel regions far from the pump (e.g., segments 4 and 7 and, to a lesser degree, segment 1) are therefore more susceptible to flooding for $\alpha_{air} = 1.3$ as compared to $\alpha_{air} = 1.5$. This observed performance improvement at $\alpha_{air} = 1.5$ suggests that even the small increase in cathode inlet pressures from $\alpha_{air} = 1.3$ to 1.5 is significant. In the next section, we will present transient studies that confirm that, for low α_{air}, the EO pump has the strongest affect for regions close to the EO pump.

Although not shown here, we also performed experiments at higher values of α_{air}. At the high stoichiometric ratio of $\alpha_{air} = 6.0$, the polarization curves with and without EO pumping were consistently nearly identical. In both cases, fuel cell performance was free of flooding in all segments and at all current densities. We again attributed this to relatively high cathode-to-pump pressure differences resulting in the removal of product water passively via the wick. Operation at this high α_{air} does not require the EO pump.

3.2. Transient results

We performed a fairly extensive set of start-up and flood-recovery experiments with our segmented cell setup. We here summarize the performance of the system as it floods (in the absence of the EO pumping) and as it recovers from severe flooding (upon activation of the EO pump). We discuss operation at $\alpha_{air} = 1.5$ and $\alpha_{H_2} = 2$, and a constant total-area-averaged current density, $\bar{I}$, of $0.5\,A\,cm^{-2}$. At these conditions, steady state operation leads to significant flooding without EO pumping and to flood-free operation when the EO pump is activated. We first purged the fuel cell with a high air flow rate to ensure a flood-

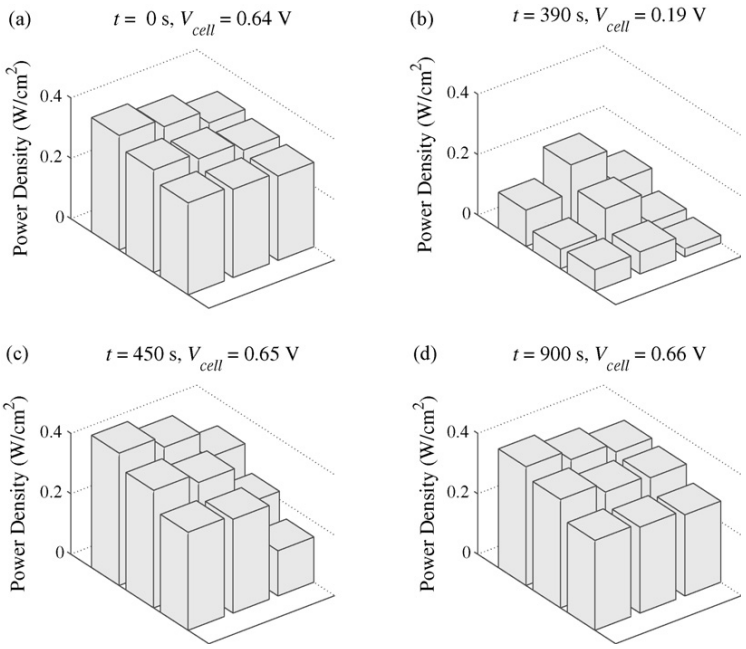

Fig. 10. Power density distribution (and cell potential) of fuel cell operated at $\alpha_{air} = 1.5$, $\alpha_{H_2} = 2.0$, and $\bar{I} = 0.5$ A at four instances in time: (a) immediately after purge, (b) after heavy flooding and immediately before EO pump is engaged, (c) at an initial stage of fuel cell recovery and (d) at the approximate steady state end condition. The corresponding cell configuration and orientation is shown in Fig. 5. Plots show transition from flood-free to near-catastrophic flooding operation, and then subsequent recovery once EO pump was engaged at 10 V (at $t = 390$ s).

free start condition. We then operated the fuel cell without EO pumping until flooding caused the cell voltage to drop below about $V_{cell} = 0.2$ V. At this point we activated the EO pump at $V_{EO} = 10$ V to initiate fuel cell recovery. We measured segment current densities and cell voltage continuously for the 15 min duration of the experiment.

Fig. 10 shows power density distribution plots at four instances in time. The bar heights on each plot represent the power density of each segment. We show segment orientation with respect to the cell configuration in Fig. 5. The plots chronologically show power distribution at the following four instances: immediately after purge ($t = 0$ s), after heavy flooding and immediately before EO pump is engaged ($t = 390$ s), during fuel cell recovery ($t = 450$ s, about 1 min after activation of the EO pump), and at the approximate steady state end condition ($t \geq 900$ s).

V_{cell} immediately following purge was 0.64 V. As expected, Fig. 10a shows that this initial fuel cell operating condition resulted in approximately uniform power distribution throughout the cell area. The power density decreased slightly with increased distance downstream. This reduction was expected and was most probably due to oxygen consumption at the cathode. After about 6 min of operation, fuel cell flooding was nearly catastrophic as fuel cell performance deteriorated significantly from the starting condition; resulting in a minimum voltage of $V_{cell} = 0.19$ V and a strongly non-uniform power distribution as shown in Fig. 10b. At this heavily flooded condition, performance losses were most significant in the outer channels of the cathode flow field and intensified with distance down stream. The manifold cross-sectional area (with respect to flow direction) was 5.0 times larger than the cross-sectional area of each parallel channel, which should result in similar pressure drops across all channels. We attribute this difference between the flooding of interior and exterior channels to the effects of in-plane temperature gradients. For example, the interior channels should experience the highest temperature and will therefore benefit from higher vapor pressure, and a resulting increase in evaporative water removal (see Hickner et al. [34]). Also, the upstream segments near the inlet header (segment 2, and to a lesser degree segments 1 and 3) produced significantly higher power densities than the remaining segments. We attribute this to the combined effects of downstream flooding and oxygen consumption. For finite power production in all segments, liquid water accumulation is expected to increase with downstream distance, while local stoichiometric ratio decreases—both limiting local reaction rates. This trend is consistent with the work of Mench and Yoon [12,13] who observed increased flooding with distance downstream in single and triple serpentine cathode flow fields.

Upon activation of the EO pump at $t = 390$ s, recovery was first observed in segments near the EO pump, followed by regions increasingly further from the EO pump. This trend of preferential water removal from areas near the pump is consistent with our steady state experiments for $\alpha_{air} = 1.3$ and 1.5, where EO pumping was unable to remove product water from far field channels. We conclude that, as anticipated, the EO pump should be located near areas most likely to flood in order to hasten flood recovery and minimize necessary pump voltage. After about 1 min of EO pumping, the fuel cell recovered considerably from the nearly catastrophic flood condition, as shown in Fig. 10c. At this point in the recovery, V_{cell} slightly exceeded the initial non-flood voltage, with an operation voltage of 0.65 V. However, current distribution was not nearly as uniform as the starting condition, as segments opposite the EO pump (segments 4 and 7, and, to a lesser degree, segment 1) still showed performance degradations indicative of flooding. The increased power here is most probably due to a minimization of ohmic losses resulting from improved membrane hydration. We hypothesize that the initial purging (to ensure no initial flooding) slightly reduced membrane humidity and conductivity.

Full fuel cell recovery was achieved about 3 min after EO pumping was first initiated. This approximate flood-free steady state condition was maintained for the remainder of the 15 min test period. This steady state operation is shown in Fig. 10d. The final operating voltage increased slightly to $V_{cell} = 0.66$ V, and revealed a uniform current distribution consistent with the flood-free operation observed initially (shown in Fig. 10a).

At all stages of the transient experiment, flow channels near the EO pump (by segments 3, 6, and 9) performed consistently better than flow channels opposite the EO pump (by segments 1, 4, and 7). This includes both extremes: the heavily flooded state with EO pump off, and the flood-free steady state end condition with an activated EO pump. At the heavily flooded state, the segment-column-averaged current densities were 0.45 A cm^{-2} for the near-pump segments and 0.29 A cm^{-2} for the segments opposite the EO pump. We attribute this to passive, wick-to-pump water removal (see Litster et al. [11] for a more detailed discussion of this issue). With EO pump activated at 10 V, these respective current densities were 0.53 and 0.46 A cm^{-2}. As shown earlier in this section and in our steady state experiments for $\alpha_{air} = 1.3$ and 1.5, the EO pump initially preferentially removes water from nearby areas in the wick flow field. Continuous use of the EO pump for higher α_{air} ensures steady state operation of the entire fuel cell without flooding.

4. Conclusion

We presented a segmented cell study for a 25 cm^2 PEMFC with a cathode-side active water management system. This system used an external EO pump hydraulically coupled to an integrated, hydrophilic porous carbon flow field (wick) for product water removal. This active water management enabled flood-free operation of a 23-channel parallel cathode flow field at low air stoichiometries. Parallel flow field structures greatly reduce the work required to drive forced air convection.

We analyzed water transport issues of the wick/pump system by studying steady state and transient current densities in nine segments. We found that, for moderate air stoichiometries ($\alpha_{air} \leq 3.0$), the fuel cell floods without EO pumping. This flooding resulted in strongly non-uniform and low average power densities. Under partially flooded conditions, performance was best in areas near the cathode inlet header, as losses due to flooding intensified with distance downstream. Inner channels consistently showed better performance than outer channels,

which we attribute to in-plane thermal gradients and the resulting increased vapor pressure for interior channels.

Transient experiments showed that upon pump activation, the fuel cell recovered to the flood-free cell voltage within 30 s. Recovery from the heavily flooded state began in regions close to the EO pump, followed by regions increasingly further from the EO pump. Steady state operation of the EO pump ensured flood-free operation for $\alpha_{air} \geq 2.0$. For these flood-free operating conditions, variations in reactant concentration dominated spatial trends in fuel cell performance, resulting, again, in a slight decrease of fuel cell performance with distance downstream. As expected, as air stoichiometry increased, downstream gradients in oxygen concentration became less significant and performance losses due to concentration reduction were minimized. Parasitic EO pump power consumption was low, ranging between 0.2 and 1% of total fuel cell power production for most operating regimes.

Acknowledgements

The authors gratefully acknowledge a Graduate Research Fellowship from the National Science Foundation for D. Strickland, and a Post-Graduate Scholarship from the Natural Science and Engineering Research Council of Canada for S. Litster.

References

[1] C.K. Dyer, J. Power Sources 106 (1–2) (2002) 31–34.
[2] M. De Francesco, E. Arato, J. Power Sources 108 (1–2) (2002) 41–52.
[3] R.K. Ahluwalia, X. Wang, A. Rousseau, R. Kumar, J. Power Sources 130 (1–2) (2004) 192–201.
[4] Q. Yan, H. Toghiani, H. Causey, J. Power Sources 161 (1) (2006) 492–502.
[5] W.R. Merida, G. McLean, N. Djilali, J. Power Sources 102 (1–2) (2001) 178–185.
[6] X. Liu, H. Guo, F. Ye, C.F. Ma, Electrochim. Acta 52 (11) (2007) 3607–3614.
[7] R.S. Gemmen, C.D. Johnson, J. Power Sources 159 (1) (2006) 646–655.
[8] G. Inoue, T. Yoshimoto, Y. Matsukuma, M. Minemoto, H. Itoh, S. Tsurumaki, J. Power Sources 162 (1) (2006) 94–104.
[9] S. Karvonen, T. Hottinen, J. Saarinen, O. Himanen, J. Power Sources 161 (2) (2006) 876–884.
[10] J.S. Yi, J.D.L. Yang, C. King, AIChE J. 50 (10) (2004) 2594–2603.
[11] S. Litster, C.R. Buie, T. Fabian, J.K. Eaton, J.G. Santiago, J. Electrochem. Soc. 154 (10) (2007) B1049–B1058.
[12] M.M. Mench, C.Y. Wang, M. Ishikawa, J. Electrochem. Soc. 150 (8) (2003) A1052–A1059.
[13] Y.-G. Yoon, W.-Y. Lee, T.-H. Yang, G.-G. Park, C.-S. Kim, J. Power Sources 118 (1–2) (2003) 193–199.
[14] G. Bender, M.S. Wilson, T.A. Zawodzinski, J. Power Sources 123 (2) (2003) 163–171.
[15] D.J.L. Brett, S. Atkins, N.P. Brandon, V. Vesovic, N. Vasileiadis, A.R. Kucernak, Electrochem. Commun. 3 (11) (2001) 628–632.
[16] S.J.C. Cleghorn, C.R. Derouin, M.S. Wilson, S. Gottesfeld, J. Appl. Electrochem. 28 (7) (1998) 663–672.
[17] S.A. Freunberger, M. Reum, A. Wokaun, F.N. Buchi, Electrochem. Commun. 8 (9) (2006) 1435–1438.
[18] A.B. Geiger, R. Eckl, A. Wokaun, G.G. Scherera, J. Electrochem. Soc. 151 (3) (2004) A394–A398.
[19] P.C. Ghosh, T. Wuster, H. Dohle, N. Kimiaie, J. Mergel, D. Stolten, J. Power Sources 154 (1) (2006) 184–191.
[20] A. Hakenjos, H. Muenter, U. Wittstadt, C. Hebling, J. Power Sources 131 (1–2) (2004) 213–216.
[21] M.M. Mench, C.Y. Wang, J. Electrochem. Soc. 150 (1) (2003) A79–A85.
[22] D. Natarajan, T. Van Nguyen, AIChE J. 51 (9) (2005) 2587–2598.
[23] M. Noponen, T. Mennola, M. Mikkola, T. Hottinen, P. Lund, J. Power Sources 106 (1–2) (2002) 304–312.
[24] N. Rajalakshmi, M. Raja, K.S. Dhathathreyan, J. Power Sources 112 (1) (2002) 331–336.
[25] I.A. Schneider, H. Kuhn, A. Wokaun, G.G. Scherer, J. Electrochem. Soc. 152 (10) (2005) A2092–A2103.
[26] J. Stumper, S.A. Campbell, D.P. Wilkinson, M.C. Johnson, M. Davis, Electrochim. Acta 43 (24) (1998) 3773–3783.
[27] H. Sun, G. Zhang, L.-J. Guo, H. Liu, J. Power Sources 158 (1) (2006) 326–332.
[28] C. Wieser, A. Helmbold, E. Gulzow, J. Appl. Electrochem. 30 (7) (2000) 803–807.
[29] C.J. Brown, J. Appl. Electrochem. 22 (7) (1992) 613–619.
[30] L.R. Czarnetzki, J. Appl. Electrochem. 19 (5) (1989) 630–636.
[31] F.N. Buchi, A.B. Geiger, R.P. Neto, J. Power Sources 145 (1) (2005) 62–67.
[32] R. Eckl, R. Grinzinger, W. Lehnert, J. Power Sources 154 (1) (2006) 171–179.
[33] J.P. Owejan, T.A. Trabold, J.J. Gagliardo, D.L. Jacobson, R.N. Carter, D.S. Hussey, M. Arif, J. Power Sources 171 (2) (2007) 626–633.
[34] M.A. Hickner, N.P. Siegel, K.S. Chen, D.N. McBrayer, D.S. Hussey, D.L. Jacobson, M. Arif, J. Electrochem. Soc. 153 (5) (2006) A902–A908.